The Fourth IEEE RAS/EMBS International Conference
on Biomedical Robotics and Biomechatronics
Roma, Italy. June 24-27, 2012

Characterization of Robotic Needle Insertion and Rotation in Artificial and *Ex Vivo* Tissues

Thomas R. Wedlick and Allison M. Okamura

***Abstract*— Accurate needle insertion to reach targets in deformable tissue relies on an understanding of tissue and needle-tissue interaction mechanics. Toward the development of clinically relevant robotic needle insertion, this work addresses (1) the differences and similarities between needle insertion into artificial and *ex vivo* tissues, and (2) the use of needle rotation data to develop needle-tissue interaction models that can be used to predict the mechanics of needle insertion. Due to challenges associated with working with living tissue, artificial and *ex vivo* tissues are often employed when modeling and testing robotic needle insertion. Force and motion data recorded during robotic needle insertion into three artificial tissues (PVC rubber, porcine gelatin, and Gelzan) and three *ex vivo* tissues (chicken breast, calf liver, and pig liver) demonstrated that the mechanics of needle insertion into artificial tissues are distinct from those of *ex vivo* tissues, due to differences in friction, stiffness, and relaxation properties. Data from needle rotation was used to fit a friction model that describes needle insertion; this approach could enable acquisition of needle-tissue interaction models for planning and control as a minimally invasive first step in a robot-assisted needle insertion procedure.**

I. Introduction

A. Motivation

Robotic needle insertion has the potential to increase precision and accuracy through implementation of novel insertion strategies, such as needle steering, which cannot be performed reliably by hand. To enable robotic needle insertion, robotic needle drivers, control strategies, path planners, mechanics models, and simulations have been developed and tested in living (*in vivo*) tissue [1–3], intact but non-living (*ex vivo*) tissue [4–10], and artificial tissue mimics [10–17]. See [18] for a review of prior work on robotic needle insertion. Due to the many challenges of working with *in vivo* tissue, most prior studies have used either *ex vivo* or artificial tissue. Despite their widespread use, the forces during robotic needle insertion into common *ex vivo* and artificial tissues have not been thoroughly compared, and the implications of tissue selection remain undetermined. The first contribution of this paper addresses this ambiguity by comparing motion and force data from robotic needle insertion into three artificial tissues (PVC rubber, porcine gelatin, and Gelzan) and three *ex vivo* tissues (chicken breast, calf liver, and pig liver) (Section IV-A). Indentation experiments were also performed to compare stiffnesses.

This work was supported by NIH grant R01 EB006435 and a NSF GRFP fellowship.

T. R. Wedlick (tomw@jhu.edu) and A. M. Okamura (aokamura@stanford.edu) are with the Mechanical Engineering Department, Johns Hopkins University, Baltimore MD, USA and the Mechanical Engineering Department, Stanford University, Stanford CA, USA.

The authors thank Dr. Marc E. Levenston for his discussion on data interpretation.

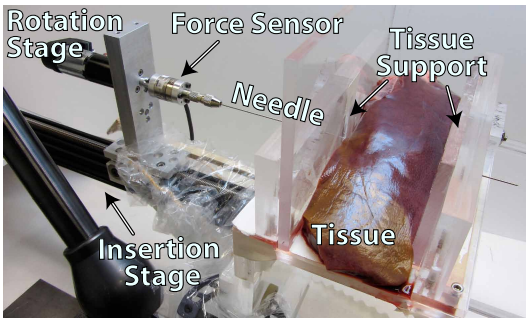

Fig. 1. Needle insertion robot used in these studies [7].

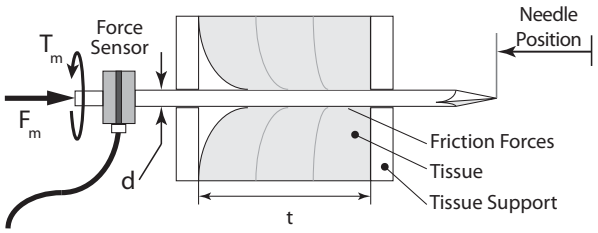

Fig. 2. Diagram defining study variables including tissue thickness (t), needle diameter (d), measured axial force (F_m), and measured rotational torque (T_m).

Force data recorded during needle insertion and retraction can be used to identify membrane puncture [3, 11] and to fit needle/tissue interaction models [5, 14], but acquiring such data necessitates moving the needle tip – risking unwanted tissue cutting or decreased insertion precision. In the second contribution of this paper, we compare data recorded during needle rotation to data from needle translation and demonstrate that models fit using rotational data are similar to models fit during needle insertion (Section IV-B). With this technique, needle rotation may be used to gather needle-tissue interaction data in a "non-destructive" way.

B. Background

Table I lists various artificial and *ex vivo* tissues previously used to study the interaction forces between a needle and tissue. Many prior studies have used these artificial tissues because they are translucent, homogeneous, and safer to handle than *ex vivo* tissues [13]. Polyvinyl chloride (PVC), a rubber-like material that lasts years with little change in appearance and mechanical properties, has often been used as a tissue mimic [10, 12, 13], but its suitability as a tissue

978-1-4577-1200-5/12/$26.00 ©2012 IEEE

TABLE I

PROPERTIES OF TESTED TISSUES

Tissue	Thicknesses (cm)	Stiffness (N/cm)	Relaxation (%)	Fall Time (s)	Max. D.R.	Min. S.N.R.
Artificial Tissue						
Plastisol PVC	2.5, 2.7, 2.9	20.6	92	46	6.8×10^{-2}	17.6
Porcine Gelatin	5.8, 5.9, 6.1	24.3	38	0.92	1.3×10^{-2}	10.9
Gelzan (Agar)	5.3, 6.1	337	0	N.A.	5.23×10^{-4}	2.36
***Ex* Vivo Tissue**						
Chicken	5.1, 5.9	5.15	41*	25*	2.8×10^{-2}	1.53
Calf Liver	5.1	0.92	41*	24*	11.1×10^{-2}	2.24
Pig Liver	5.2, 5.7	1.18	48*	34*	23.1×10^{-2}	7.60

Notes: *Asterisk (*) indicates that forces did not fully settle in* 60 *seconds.*
Fall time is the time required for the insertion force to decay to 90% *of its final measured value.*
Deformation ratio (D.R.) was defined for each insertion as: $D.R. = \frac{max(|Normalized\ Force|)}{Stiffness}$.
Signal-to-Noise ratio (S.N.R.) was defined for each insertion as: $S.N.R. = \frac{max(|Normalized\ Force|)}{max(|Difference\ from\ Mean\ Insertion\ Force|)}$.

surrogate has not been established. Organic artificial tissues such as gelatin from pig skin and bone [10, 13, 16] and agar [13–15] have also been used as tissue mimics; however, their needle insertion properties have not been thoroughly compared to other artificial and real tissues. These organic artificial tissues are safer to handle than *ex vivo* tissues, but they have a limited storage life due to spoilage. Furthermore, the properties of porcine gelatin are not always stable at room temperature.

Various *ex vivo* tissues have also been used as *in vivo* tissue mimics. Clinician trainees often use turkey breast to mimic human breast for needle insertion training, though mechanical differences between the two tissues have been noted [19, 20]. Chicken breast [10], bovine liver [5], and pig liver [6, 8] have also been used to model the interaction between needles and tissue. Clinicians have reported that needle insertion into living human tissue feels more similar to pig *ex vivo* tissue, than the other *ex vivo* tissues [20]. All of these tissues contain internal structures which make them a less repeatable material in which to test needle insertion strategies [2, 7], quickly spoil, and are likely to contain harmful bacteria. The interaction forces between a needle and these *ex vivo* tissues have not been previously compared.

II. METHODS

A. Tissue Acquisition and Preparation

The artificial tissues were prepared to be similar to artificial tissues used in [10], [14], and [15]. The rubber specimen was constructed with four parts Plastisol rubber to one part Plastisol softener (M-F Manufacturing, Inc). The Gelzan sample was prepared with 5.7% by weight Gelzan powder (CP Kelco Co.), which is chemically equivalent to Gelrite, and tap water. The porcine gelatin was prepared with 16% by weight porcine gelatin (300g bloom-strength from Sigma-Aldrich, Inc.) and tap water.

The *ex vivo* tissue samples were acquired fresh from local meat suppliers. The edges of the tissue samples were trimmed to be parallel so that the tissue samples could be restrained in the direction of insertion by two pieces of plastic with small holes through which the needle passed (Figures 1 and 2). Trimming the *ex vivo* tissue samples removed organ membranes, which was desirable since this study is concerned with the forces between a needle and specific organ tissue, not the surrounding membranes; however, the original tissue thicknesses were maintained as much as possible to represent the geometry of the intact organs.

All the tissue samples were allowed to reach room temperature prior to experimentation except for the porcine gelatin which, following the approach used in [16], was removed from a refrigerator and allowed to sit for two hours prior to experimentation. To maintain its firmness, it was not allowed to warm to room temperature, and its behavior did not noticeably change throughout the experiments.

B. Experiments

Three types of experiments were performed with each tissue type: indentation, needle insertion, and needle rotation. Each experiment used a needle steering robot (Figure 1) [7] to generate and acquire motion and force data. The system consisted of a needle holder attached to a six-degree-of-freedom force sensor (Nano 17 from ATI, Inc.) mounted to a needle rotation stage. This assembly rode on a linear needle translation stage. Forces and torques were recorded at 20kHz, linear and rotational positions were recorded at 1kHz, and the robot controllers ran at 500Hz.

During indentation experiments, reaction forces were recorded while a blunt, 4.77mm-diameter cylindrical stainless steel punch was indented into tissue at 1mm/s and then retracted. The punch was not indented far enough to cause tissue fracture.

During needle insertion experiments, the axial insertion force was recorded while a 0.98mm-diameter stainless steel stylet with a Framseen (triangular pyramid) tip from an 18-gauge prostate brachytherapy seeding needle (product number PSS1820AT from Worldwide Medical Technologies, LLC) was inserted into tissue. Each insertion experiment began with the needle initially outside the tissue, which was held in place by two plastic plates with small holes through which the needle could pass (Figure 2). The needle was inserted through the holes and tissue at 1mm/s, which is within the range of speeds used in epidural needle insertion [21], until the needle tip extended 5cm beyond the tissue (Figure 3). The needle was held stationary for 60 seconds so the tissue could relax. Then, the needle was cyclically

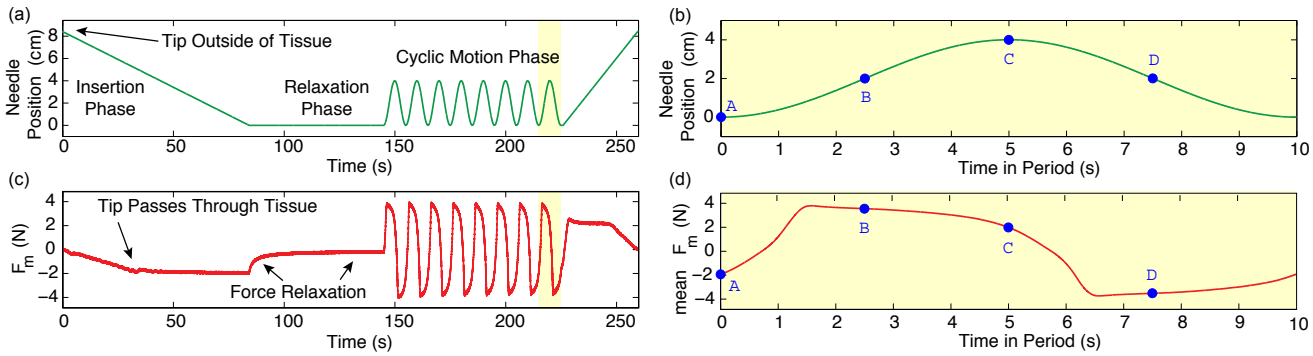

Fig. 3. Needle motion (a), an expanded view of the oscillation period (b), measured forces (c), and the mean cyclic force (d) during a needle insertion experiment into PVC tissue. See Figure 2 for variable definitions. Points at the start, one-quarter, one-half, and three-quarters of the period are denoted by the points labeled A,B,C, and D, respectively. The mean force was computed by averaging the last five periods of oscillation.

retracted and inserted with a 4cm peak-to-peak amplitude. Experiments were conducted using sinusoidal motion with 10s and 45s periods and constant-velocity motion at 1.5, 2.5, 7.5, or 12.5mm/s. Data was recorded for between 8 to 20 cycles before retracting the needle from the tissue; more cycles were used for *ex vivo* tissues which were non-homogeneous and whose frictional properties displayed greater variability.

Needle rotation experiments were identical to needle insertion experiments except that sinusoidal needle rotation with a 390° peak-to-peak amplitude and 3.6 second periods replaced linear needle oscillation. This period was selected so that rotational velocities were comparable, using a relation presented in the following section, to the velocities measured during sinusoidal needle motion with 45s periods and this amplitude was chosen to avoid collision between the force sensor cable and the needle during rotation.

Figure 3 shows the motion and forces during an insertion experiment in PVC tissue. An isolated view of one period of cyclic motion is labeled A, B, C, and D at the points starting, one-quarter, one-half, and three-quarters through the period. At least five needle experiments were conducted for each tissue material and for each variation of needle motion, resulting in at least 35 needle experiments for each tissue. The tissue was moved between each insertion experiment to ensure that the needle did not reenter a prior needle tract.

C. Data Analysis

In these experiments, needle inertia and torsion were negligible because the needle was relatively light and stiff. To account for different tissue thicknesses, force and torque measurements were normalized by dividing them by the thickness of the tissue through which the needle passed, t (Figure 2). In order to compare linear needle motion to rotational needle motion, rotational positions and velocities were multiplied by the needle radius to convert them to their linear equivalents. The relationship between the equivalent linear normalized force, F_{eq}, and the torque measurement, T_m, was

$$F_{eq} = \frac{2T_m}{d \times t}. \quad (1)$$

The position measurements were differentiated to determine the needle velocity, which was smoothed with a low-pass filter with a 10Hz cutoff frequency. To eliminate effects of linear slide mechanics, such as friction and vibration, noise was reduced by smoothing the force measurements with a low-pass filter with a 0.5Hz cutoff frequency, which did not add noticeable lag or remove any salient features from the signals. Position, velocity, and force values were decimated to be at a consistent 500Hz.

Sinusoidal and constant-velocity cyclic motions were used to elicit forces and torques associated with needle motion. Normalized forces from the last five periods of oscillation were segmented and averaged between those five cycles to determine a representative mean interaction force profile for a specific needle motion and tissue (Figure 3(d)). This was then

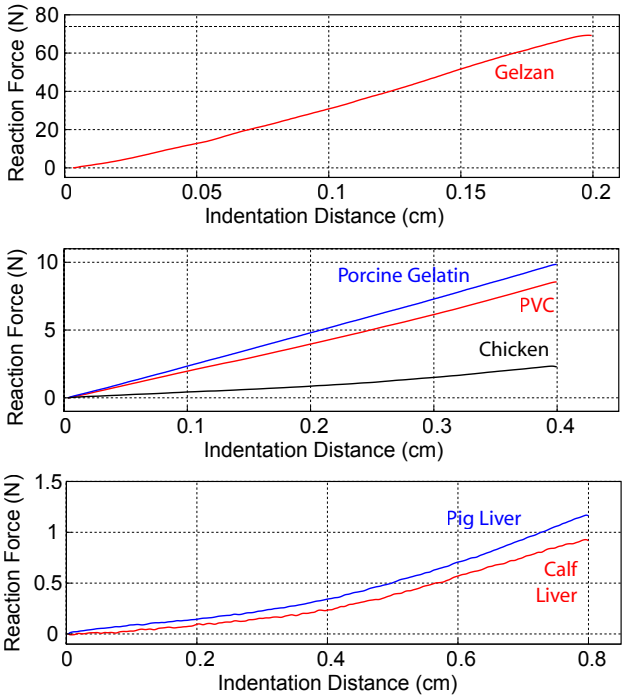

Fig. 4. Forces recorded during indentation experiments.

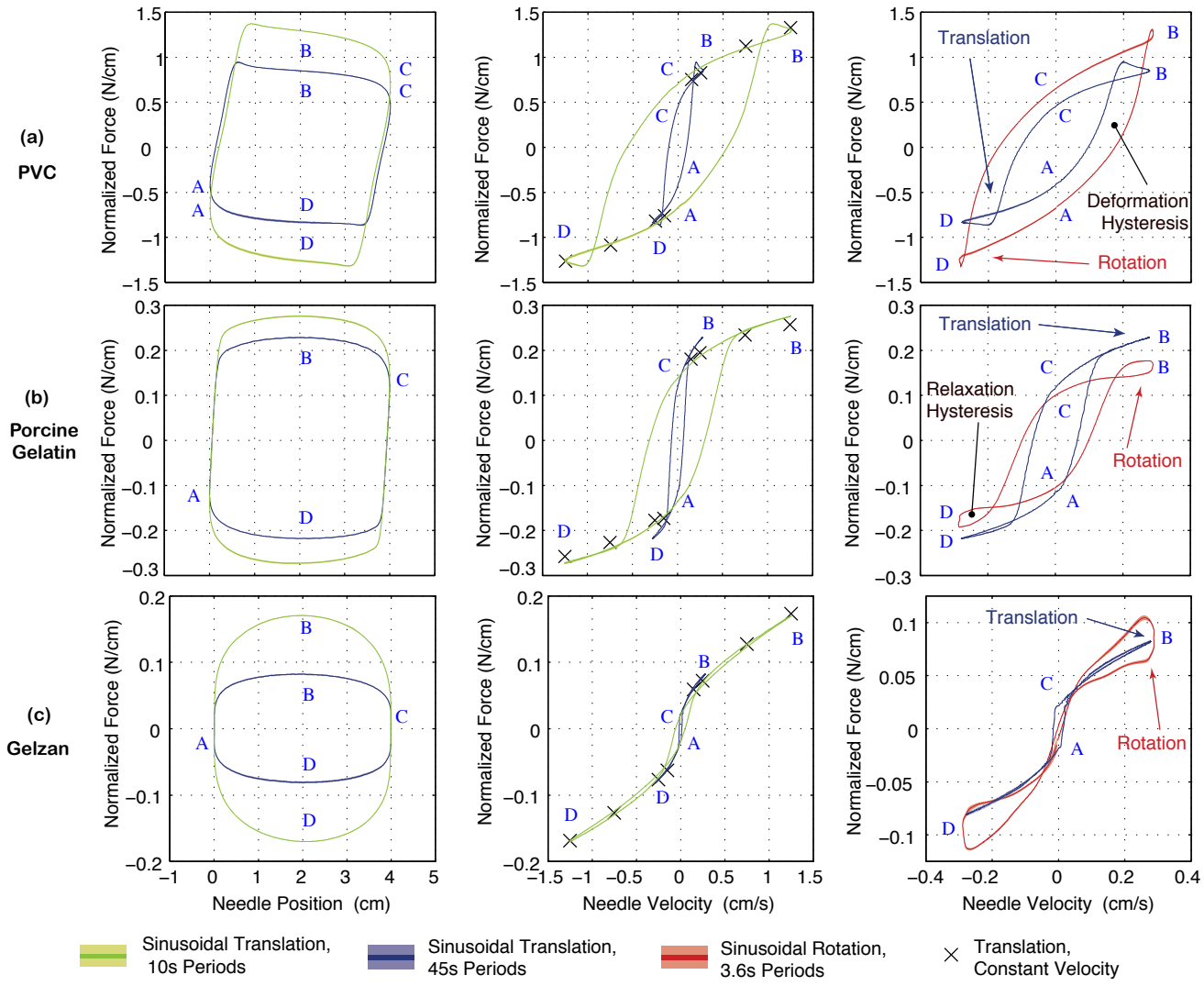

Fig. 5. Mean interaction force data between a needle and the artificial tissues during insertion experiments. The mean force during sinusoidal motion is indicated and the line thickness corresponds to two standard deviations of the mean force during each insertion experiment. The data points identified by ×'s are the mean force during the last quarter of the constant-velocity insertion periods. Rotational motion and examples of both types of hysteresis loops are labeled.

averaged with the mean profile of all other experiments (at least five) into the same tissue with the same needle motion to calculate a representative force profile. The differences between the measured force and the mean force resulting from each experiment with the same tissue and motion were combined to create a standard deviation profile. This represented the variability within a single insertion experiment from the mean force profile of that experiment. The resulting mean behaviors and standard deviations are presented in the following section.

III. Results

Data recorded during the indentation experiments are presented in Figure 4. A linear stiffness was fit to this data (Table I), which only provides an approximate method of comparing tissue stiffnesses since these are viscous hyperelastic materials [10, 13] and all the materials displayed hysteresis.

During the needle insertion and rotation experiments, after the needle was initially inserted through the tissue it was held stationary for 60s to observe insertion force relaxation. The relaxation characteristics of each tissue are presented in Table I. Except for Gelzan, all the materials appreciably relaxed insertion forces but with different rates and magnitudes. An exponential model did not suitably describe any of the relaxation behaviors, so the 90% fall times were reported.

Figures 5 and 6 show how mean force varied with needle motion for artificial and *ex vivo* tissues, respectively. The left column in each figure demonstrates how force varied with needle position during sinusoidal motion, and the two right columns show how the force varied with velocity. The data points indicated by × represent the data recorded during constant-velocity cyclic motion. The rightmost column compares needle rotation to translational insertion.

The force profiles had some common features, such as higher needle speeds generally corresponding to increased

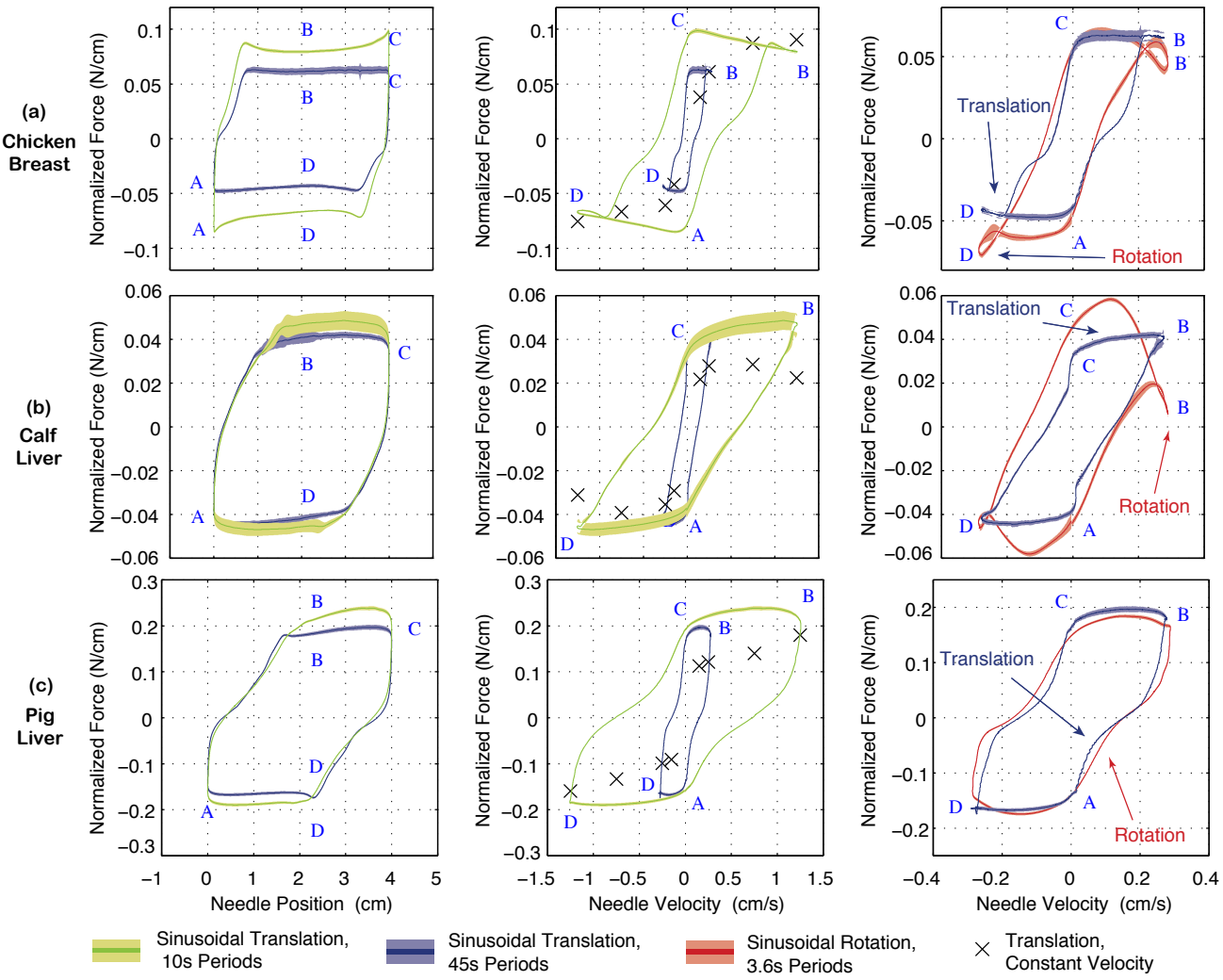

Fig. 6. Mean interaction force data between a needle and the *ex vivo* tissues during insertion experiments. The mean force during sinusoidal motion is indicated and the line thickness corresponds to two standard deviations of the mean force during each insertion experiment. The data points identified by ×'s are the mean force during the last quarter of the constant-velocity insertion periods. Rotational motion is labeled.

forces and the presence of hysteresis loops. Significant differences between the tissues included the magnitude of the interaction forces and the degree of hysteresis. The reasons for these commonalities and differences are discussed in the following section.

IV. Discussion

A. Explanation of Interaction Forces

The force measured at the base of the needle is the summation of the interaction forces that occur along the needle shaft (Figure 2), which are influenced by the friction resisting relative motion between the needle and the tissue, and tissue deformation caused by frictional forces. This section discusses these two sources of interaction force behavior and how they resulted in the behaviors seen in Figures 5 and 6.

We define the deformation ratio of each experiment as the ratio of the maximum normalized force during cyclic motion to the linear stiffness of each material. This is a qualitative non-dimensional indicator of the amount of tissue deformation during each experiment. The maximum ratio for each tissue is listed in Table I. Gelzan possessed the smallest deformation ratio, was the stiffest tissue, and did not perceivably deform during experimentation; all other tissues deformed. The PVC and gelatin tissues were similarly stiff but had different frictional properties, which resulted in both different magnitudes of interaction force and extent of tissue deformation. During experimentation, the *ex vivo* tissues deformed the most and also had the largest deformation ratios. Tissue deformation was one cause of hysteresis in the interaction behaviors.

Hysteresis manifested as two types of loops in the force-velocity plots in Figures 5 and 6, each type originating from a different source. Tissue deformation resulted in hysteresis loops centered about the origin and intersecting points A and C, when the needle was momentarily stationary. Gelzan, which essentially did not deform, was the only tissue to negligibly display this form of hysteresis.

Interaction force relaxation caused the other type of hysteresis in the figures, which can be seen as a pair of symmetric loops intersecting points B and D in the force-velocity figures. Interaction force relaxation stemmed from two sources: dissipative stress relaxation within the tissue and slippage between the needle and the tissue allowing the tissue to reach a lower stress configuration. All the tissue materials were viscoelastic, but relaxation hysteresis was only apparent when the relaxation time was similar to the length of the oscillation period and after tissue deformation had reached its maximum value. The relaxation was apparent in the interaction behavior resulting from constant velocity motion, but its effects during sinusoidal oscillation were more complex. To understand this hysteresis, it is worthwhile to sequentially step through half of a period of cyclic motion.

At point A, the needle was momentarily stationary and the tissue may (PVC, gelatin, *ex vivo*) or may not (Gelzan) have been deflected from prior needle motion. If it was previously deformed, then that deformation was quickly relieved as the needle began to move from point A to point B, a result also described in [13]. Depending on the tissue, the return to an undeformed state may be an inflection point on the force-position plots in Figures 5 and 6. As needle motion continued from point A towards point B and then point C, frictional forces caused tissue deformation. Depending on the tissue and the motion, a dynamic equilibrium was eventually reached between the friction and the tissue deformation. For some tissues, after this point insertion force relaxation reduced the interaction force, causing hysteresis loops. For this to be noticeable, force relaxation must have continued to occur after tissue deformation, but it must not have been so slow that it had no effect before reaching point C.

PVC, which was capable of a large amount of relaxation over a relatively long period of time (92% in over 46s, see Table I), displayed hysteresis loops when the needle oscillated in 45s, 10s, and 3.6s periods. Because porcine gelatin relaxes so quickly, these loops were not noticeable with 45s or 10s period linear oscillation but were noticeable with 3.6s period rotational oscillation. This form of relaxation was pronounced with needle rotation in Gelzan. It is hypothesized that Gelzan, being the stiffest material, had the fastest relaxation time – but the frictional forces resulting from linear motion were not large enough to cause significant tissue deformation to be noticeably relaxed over 45s or 10s periods. During rotational motion, which had a smaller period, fast relaxation played more of a role, resulting in more apparent hysteresis loops. The *ex vivo* tissues deformed significantly during these experiments, often not reaching a dynamic equilibrium, which accounts for their less pronounced hysteresis loops.

While all the interaction behaviors displayed some common features, such as hysteresis, there were significant differences between the *ex vivo* and the artificial tissues. The measured forces from *ex vivo* tissue varied more with tissue deformation than with the needle's velocity. The *ex vivo* tissue was also heterogeneous and therefore had a lower signal to noise ratio (S.N.R.), which was defined as the highest difference from the mean force profile for a specific insertion divided by the largest normalized force measured during that insertion (Table I).

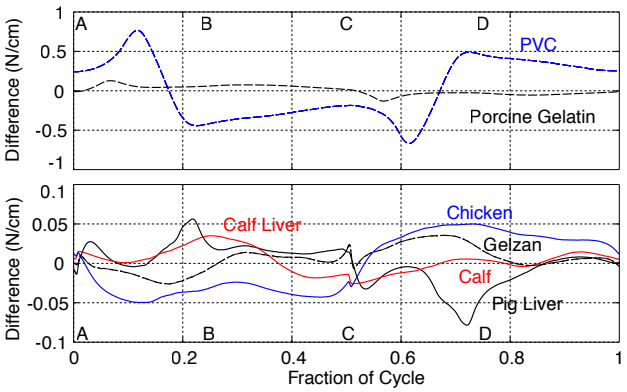

Fig. 7. Difference between forces during translation and equivalent rotational forces during oscillation. Note scale differences in the top and bottom plots.

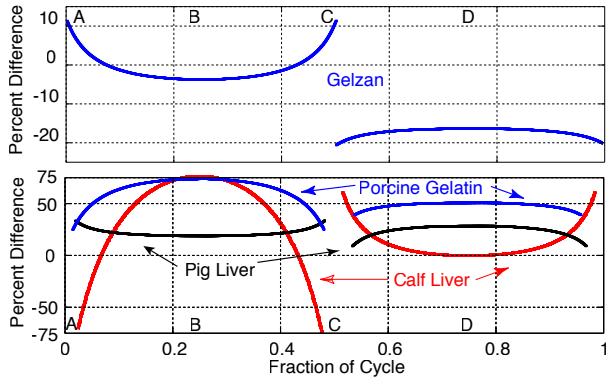

Fig. 8. Percent difference between the forces predicted during sinusoidal motion with a 45s period and 4cm peak-to-peak amplitude by the modified Karnopp models fit to translational data and to rotational data.

TABLE II

MODIED KARNOPP MODEL PARAMETERS

Tissue	Motion	C_p N/mm	b_p N s/mm^2	C_n N/mm	b_n N s/mm^2
Artificial Tissue					
Gelzan	Insertion	0.249	21.8	0.245	21.4
	Rotation	0.223	23.9	0.303	24.9
***Ex* Vivo Tissue**					
Chicken	Insertion	0.141	18.7	0.134	12.8
	Rotation	0.240	11.0	0.072	22.3
Calf Liver	Insertion	0.033	13.9	0.119	11.51
	Rotation	0.195	−0.19	0.041	14.6
Pig Liver	Insertion	0.294	48.2	0.117	49.1
	Rotation	0.187	42.6	0.174	34.5

Note: *For model and parameter and definitions, see [5].*

B. Needle Rotation to Facilitate Insertion Modeling

Figure 7 shows differences between insertion and rotation forces for all tissues. For *ex vivo* tissues, the mean force profiles resulting from needle rotation were very similar to the mean insertion force profiles for a given tissue. Only one of the artificial tissues, Gelzan, exhibited this similarity.

The *ex vivo* tissue result is promising because it suggests that needle rotation can be used to gather relevant information for modeling needle insertion in biological tissue. This could be used to improve planning and control, or to enhance a clinician's perception of tip forces using an approach similar to that of Koseki et al. [11], in which needle tip forces were separated from needle shaft forces using a special mechanism. The needle shaft forces may be directly measured through needle shaft rotation, or they may be determined with a model fit using needle rotation. Needle rotation provides useful information without progressing the needle tip within the tissue.

Prior studies have considered fitting a force model in real time while a needle was inserted into tissue [2, 14]. These approaches required accurate initial guesses of model parameters for estimator convergence [2]. This and prior studies have demonstrated that the forces during insertion into biological tissue can vary significantly, which may render these estimation schemes unreliable or necessitate undesirably deep insertions to yield parameter convergence. The suggested approach of using needle rotation in an estimator to fit needle insertion models would not necessitate such long insertions to generate a large amount of information on how a needle interacts with tissue.

To demonstrate the correlation between translational and rotational data, the modified Karnopp friction model [5] was fit to the force data from Gelzan and the *ex vivo* tissues (Table II), and the resulting predictions were compared (Figure 8). While the data presented in Figures 5 and 6 suggest that a modified Karnopp model cannot fully capture the complex force profiles measured for most tissues, the Gelzan result provides a proof-of-concept that one can use rotational motion data to fit a model for linear motion – given an appropriate model.

V. Conclusions

This paper experimentally examined the needle shaft forces resulting from linear and rotational constant-velocity and sinusoidal motion in six common tissue mimics (three artificial and three *ex vivo*). Significant differences were found between needle-tissue interaction behaviors, and none of the artificial tissues closely mimicked the *ex vivo* tissues. Developing a more realistic artificial tissue is one direction of future work and might be achieved by mixing different artificial material ingredients to combine their properties.

It was shown that torque measured during needle rotation is related to needle shaft force during insertion in *ex vivo* tissue, which may facilitate needle insertion force modeling and novel insertion techniques that improve a surgeon's perception of the forces at the needle tip. A modified Karnopp friction model was fit to the data in this paper, but that model could not fully describe the complex behavior of *ex vivo* tissue. With the development of a more suitable model, the benefit of using needle rotation data to enhance needle insertion procedures can be demonstrated.

References

[1] L. Barbé, *et al.*, "Needle Insertions Modeling: Identifiability and Limitations," *Biomedical Signal Processing and Control*, vol. 54, no. 3, pp. 191–198, 2007.

[2] L. Barbe, *et al.*, "In Vivo Model Estimation and Haptic Characterization of Needle Insertions," *The International Journal of Robotics Research*, vol. 26, no. 11-12, pp. 1283–1301, Nov. 2007.

[3] T. Washio and K. Chinzei, "Needle Force Sensor, Robust and Sensitive Detection of the Instant of Needle Puncture," in *Medical Image Computing and Computer Assisted Intervention*, ser. Lecture Notes in Computer Science, C. Barillot, D. R. Haynor, and P. Hellier, Eds., vol. 3217. Berlin, Heidelberg: Springer Berlin Heidelberg, 2004, pp. 113–120.

[4] H. Kataoka, *et al.*, "Measurement of the Tip and Friction Force Acting On a Needle During Penetration," *International Conference on Medical Image Computing and Computer Assisted Intervention*, vol. 2488, pp. 216–223, 2002.

[5] A. M. Okamura, C. Simone, and M. D. O'Leary, "Force Modeling for Needle Insertion Into Soft Tissue." *IEEE Transactions on Bio-Medical Engineering*, vol. 51, no. 10, pp. 1707–16, Oct. 2004.

[6] J. T. Hing, A. D. Brooks, and J. P. Desai, "A Biplanar Fluoroscopic Approach for the Measurement, Modeling, and Simulation of Needle and Soft-Tissue Interaction." *Medical Image Analysis*, vol. 11, no. 1, pp. 62–78, Feb. 2007.

[7] A. Majewicz, *et al.*, "Evaluation of Robotic Needle Steering in Ex Vivo Tissue," in *IEEE International Conference on Robotics and Automation*, vol. 67. IEEE, 2010, pp. 2068–2073.

[8] Y. Kobayashi, T. Sato, and M. G. Fujie, "Modeling of Friction Force Based on Relative Velocity Between Liver Tissue and Needle for Needle Insertion Simulation," *IEEE Engineering in Medicine and Biology Society. Conference*, pp. 5274–8, Jan. 2009.

[9] Y. Yang, *et al.*, "Insertion force in Manual and Robotic Corneal Suturing," *International Journal of Medical Robotics and Computer Assisted Surgery*, Oct. 2011.

[10] K. B. Reed, A. M. Okamura, and N. J. Cowan, "Modeling and Control of Needles with Torsional Friction." *IEEE Transactions on Bio-Medical Engineering*, vol. 56, no. 12, pp. 2905–16, Dec. 2009.

[11] Y. Koseki, D. D. Lorenzo, and K. Chinzei, "Coaxial Needle Insertion Assistant for Epidural Puncture," in *IEEE/RSJ International Conference on Intelligent Robots and Systems*, 2011, pp. 2584–2589.

[12] E. Dehghan, *et al.*, "Parameter Identification for a Needle-Tissue Interaction Model," in *IEEE Engineering in Medicine and Biology Society Conference*, vol. 2007, Jan. 2007, pp. 190–3.

[13] T. Podder, *et al.*, "Robotic Needle Insertion in Soft Material Phantoms: An Evaluation of Properties of Commonly Used Soft Materials," in *International Conference on Biomedical Engineering*, 2005, pp. 4–7.

[14] A. Asadian, M. R. Kermani, and R. V. Patel, "A Novel Force Modeling Scheme for Needle Insertion Using Multiple Kalman Filters," *IEEE Transactions on Instrumentation and Measurement*, vol. 61, no. 2, pp. 429–438, Feb. 2012.

[15] A. Asadian, R. V. Patel, and M. R. Kermani, "A Distributed Model for Needle-Tissue Friction in Percutaneous Interventions," *IEEE International Conference on Robotics and Automation*, pp. 1896–1901, 2011.

[16] S. Badaan, *et al.*, "Does Needle Rotation Improve Lesion Targeting?" *The International Journal of Medical Robotics and Computer Assisted Surgery*, vol. 7, no. 2, pp. 138–47, June 2011.

[17] V. Mallapragada, N. Sarkar, and T. K. Podder, "Toward a Robot-Assisted Breast Intervention System," *IEEE/ASME Transactions on Mechatronics*, vol. 16, no. 6, pp. 1011–1020, Dec. 2011.

[18] N. Abolhassani, R. Patel, and M. Moallem, "Needle Insertion into Soft Tissue: a Survey." *Medical Engineering & Physics*, vol. 29, no. 4, pp. 413–31, May 2007.

[19] C. D. Lehman and T. Aikawa, "MR-Guided Vacuum-Assisted Breast Biopsy: Accuracy of Targeting and Success in Sampling in a Phantom Model." *Radiology*, vol. 232, no. 3, pp. 911–4, Sept. 2004.

[20] G. Hocking, S. Hebard, and C. H. Mitchell, "A Review of the Benefits and Pitfalls of Phantoms in Ultrasound-Guided Regional Anesthesia," *Regional Anesthesia and Pain Medicine*, vol. 36, no. 2, pp. 162–70, 2011.

[21] L. L. H. Holton, "Force Models for Needle Insertion Created from Measured Needle Puncture Data," in *Medicine Meets Virtual Reality*, J. D. Westwood, Ed. IOS Press, 2001, pp. 180–186.